BAMS Article

Opportunities and Barriers for Skillful Subseasonal Prediction of East Asian Summer Precipitation

Fei Liu,[a] Jiahui Zhou,[a,j] Bin Wang,[b] Jeremy Cheuk-Hin Leung,[c,k] Deliang Chen,[d,l] Zhongda Lin,[e] In-Sik Kang,[f] Qingchen Chao,[g] Zongjian Ke,[g] Ke Fan,[a] Boqi Liu,[h] Gang Huang,[e] Pang-chi Hsu,[i] and Wenjie Dong[a]

KEYWORDS: Rossby waves; Subseasonal variability; Hindcasts; Numerical weather prediction/ forecasting; Short-range prediction

ABSTRACT: Accurate subseasonal (2–8 weeks) prediction of monsoon precipitation is crucial for mitigating flood and heatwave disasters caused by intraseasonal variability (ISV). However, current state-of-the-art subseasonal-to-seasonal (S2S) models have limited prediction skills beyond 1 week when predicting weekly precipitation. Our findings suggest that predictability primarily arises from strong ISV events, and the prediction skills for ISV events depend on the propagation stability of preceding signals, regardless of models. This allows us to identify opportunities and barriers (OBs) within S2S models, clarifying what the models can and cannot achieve in ISV event prediction. Focusing on the complex East Asian summer monsoon (EASM), we discover that stable propagation of Eurasian and tropical atmospheric wave trains toward East Asia serves as an opportunity. This opportunity offers a 1-week leading prediction skill of up to 0.85 and skillful prediction up to 13 days ahead for 43% of all ISV events. However, the Tibetan Plateau barrier highlights the limitation of EASM predictability. Identifying these OBs will help us gain confidence in making more accurate subseasonal prediction.

SIGNIFICANCE STATEMENT: Accurate subseasonal prediction (2–8 weeks) is urgently needed to facilitate effective disaster prevention, application of renewable energy, logistical planning, agricultural production, and decision-making. Current scientific research and practical applications typically focus on predicting all ISV events, which renders the low-average prediction skill relatively less helpful. In response, we propose an innovative idea for performing subseasonal prediction: predicting only what the models can accurately predict. The central idea is to identify the types of ISV events in which the model exhibits high prediction skills (opportunities) and those where the model's skills are limited (barriers). Compared to the average forecast skill of all events, accurate predictions of specific events can be more beneficial to us.

DOI: 10.1175/BAMS-D-24-0055.1

Corresponding authors: Fei Liu, liufei26@mail.sysu.edu.cn; Wenjie Dong, dongwj3@mail.sysu.edu.cn

Supplemental information related to this paper is available at the Journals Online website: https://doi.org/10.1175/BAMS-D-24-0055.s1.

Manuscript received 17 February 2024, in final form 14 August 2024, accepted 3 October 2024

© 2024 American Meteorological Society. This published article is licensed under the terms of the default AMS reuse license. For information regarding reuse of this content and general copyright information, consult the AMS Copyright Policy (www.ametsoc.org/PUBSReuseLicenses).

Unauthenticated | Downloaded 11/22/24 07:15 PM UTC

AFFILIATIONS: [a] School of Atmospheric Sciences, Sun Yat-Sen University, Key Laboratory of Tropical Atmosphere-Ocean System Ministry of Education, and Southern Marine Science and Engineering Guangdong Laboratory, Zhuhai, China; [b] Department of Atmospheric Sciences and International Pacific Research Center, University of Hawai'i at Mānoa, Honolulu, Hawaii; [c] Guangzhou Institute of Tropical and Marine Meteorology, Guangdong Provincial Key Laboratory of Regional Numerical Weather Prediction, China Meteorological Administration, Guangzhou, China; [d] Department of Earth Sciences, University of Gothenburg, Gothenburg, Sweden; [e] State Key Laboratory of Numerical Modeling for Atmospheric Sciences and Geophysical Fluid Dynamics, Institute of Atmospheric Physics, Chinese Academy of Sciences, Beijing, China; [f] State Key Laboratory of Satellite Ocean Environment Dynamics, Second Institute of Oceanography, Ministry of Natural Resources, Hangzhou, China; [g] National Climate Center, China Meteorological Administration, Beijing, China; [h] State Key Laboratory of Severe Weather (LaSW), Chinese Academy of Meteorological Sciences, China Meteorological Administration, Beijing, China; [i] Key Laboratory of Meteorological Disaster of Ministry of Education, Joint International Research Laboratory of Climate and Environment Change, Collaborative Innovation Center on Forecast and Evaluation of Meteorological Disasters, Nanjing University of Information Science and Technology, Nanjing, China; [j] Guangdong meteorological data center, Guangzhou, China; [k] Hunan Institute of Advanced Technology, Changsha, China; [l] Department of Earth System Sciences, Tsinghua University, Beijing, China

1. Introduction

The record-breaking East Asian summer monsoon (EASM) precipitation in 2020 had a widespread impact on millions of people across East Asia, resulting in more than 260 human casualties and an economic loss exceeding 16 billion U.S. dollars in China, Japan, and South Korea (Hirockawa et al. 2020; Takaya et al. 2020; Wei et al. 2020; KMA 2021; Park et al. 2021). In 2022, the high-intensity and prolonged heat wave and extreme precipitation also hit different parts of East Asia due to internal variability and global warming, leading to a direct economic loss of 4.7 billion U.S. dollars in China (He et al. 2023; Jiang et al. 2023; Sheng et al. 2023). These extreme precipitation and heat wave events, influenced by intraseasonal variability (ISV), often manifest as a series of wet and dry pulses on the subseasonal time scale (Zhang 2013; Hsu et al. 2016; Ding et al. 2021; Liu et al. 2022), and have become more frequent and intense associated with the global warming (Meehl and Tebaldi 2004; Liu et al. 2022).

Accurate prediction of precipitation on the subseasonal time scale is crucial for various sectors, including renewable energy application, disaster prevention, logistical planning, agricultural production, and decision-making (Webster and Hoyos 2004). Current state-of-the-art subseasonal-to-seasonal (S2S) prediction models, however, exhibit a relatively low prediction skill (with a correlation coefficient < 0.5) beyond 1 week for weekly monsoon precipitation anomaly forecasts (Li and Robertson 2015; de Andrade et al. 2019), particularly for the EASM (Liu et al. 2022).

In the pursuit of subseasonal prediction, researchers have attempted to identify strategic windows of opportunity that provide specific climate phenomena or conditions for a predictable signal above the weather noise (Sigmond et al. 2013; National Academies of Sciences, Engineering, and Medicine 2016; Lim et al. 2019; Mariotti et al. 2020; Singh et al. 2024). However, accurately predicting EASM ISV poses a particular challenge due to the complex tropical–extratropical interaction and Tibetan Plateau's influence (Stan et al. 2017; Liu et al.

Unauthenticated | Downloaded 11/22/24 07:15 PM UTC

2022). Multiple factors contribute to the large magnitude of EASM ISV (Ren et al. 2022), including the northwestward-propagating boreal-summer intraseasonal oscillation (Chen et al. 2001; Mao and Chan 2005), Tibetan Plateau heating (Y. Liu et al. 2020), the quasi-biweekly oscillation (Yang et al. 2010; Hsu et al. 2016), and the southeastward-propagating mid-to-high latitude wave trains (Yang et al. 2017; Gao et al. 2018).

To date, it remains unclear whether the current state-of-the-art dynamic prediction models can effectively capture these preceding signals to enhance subseasonal prediction for each EASM ISV event. Addressing the above issue could help enhance the subseasonal prediction skill for some ISV events, thereby improving its practical application. Our strategy is to differentiate the capabilities of current state-of-the-art S2S prediction models (the opportunities) from their limitations (the barriers) and gain a deeper understanding of why S2S models succeed in capturing certain opportunities and yet fail to overcome specific barriers. Specifically, we first categorized ISV events into well-predicted and poorly predicted events based on the model performance. Then, we constructed the observed preceding signals for these two types of events by examining explicable physical processes, which can be considered as the opportunities and barriers (OBs) for S2S model prediction. When the initial signals resemble the opportunities, it indicates a higher accuracy and confidence level in the prediction results, providing a reliable signal for us to raise the alarm for potential disasters. The identification of prediction barriers also underscores the limitation of monsoon predictability.

Here, we used the wide-ranging database from 12 models in the S2S prediction project, which was jointly launched by World Weather Research Programme (WWRP) and World Climate Research Programme (WCRP) to meet the increasing need for accurate S2S prediction (Vitart et al. 2017). The longest reforecasts (hindcasts) can extend up to 65 days.

2. Data and methods

a. Observation and prediction data. We used daily Climate Prediction Center (CPC) global precipitation data with a high resolution of 0.5° × 0.5°, provided by the National Oceanic and Atmospheric Administration (NOAA) (Xie et al. 2007), owing to their extensive temporal coverage extending from 1979 to 2021 and their good ability in capturing EASM ISV (F. Liu et al. 2020). To represent tropical large-scale organized deep convection, daily outgoing longwave radiation (OLR) data with a resolution of 2.5° × 2.5° provided by the NOAA were used (Liebmann and Smith 1996). Daily winds and geopotential height at 200 hPa, obtained from the National Centers for Environmental Prediction (NCEP) Reanalysis II dataset (Kanamitsu et al. 2002), were used to composite the extratropical intraseasonal signal. The study period covered the boreal summer from 1979 to 2021. All EASM ISV events during broad summer season from May to September were defined and analyzed. The seasonal evolution of EASM ISV, with a preceding signal evolving from mid-to-high latitudes in early summer and from the tropics in late summer (F. Liu et al. 2020), was not the focus here and should be investigated in the near future.

To study the subseasonal prediction of EASM precipitation, the hindcasts of precipitation from 12 global prediction systems, which participated in the S2S prediction project (Vitart et al. 2017), were investigated (Table 1). These models had different ensemble sizes for their hindcasts, and the multiensemble mean of each model was used. To make a fair comparison between other S2S models with the European Centre for Medium-Range Weather Forecasts (ECMWF) model, which exhibited the best prediction skill and conducted hindcast twice per week (on Monday and Thursday), we also adopted the same frequency for the Institute of Atmospheric Physics (IAP), Chinese Academy of Sciences, and NCEP models, both of which provided daily hindcasts.

Unauthenticated | Downloaded 11/22/24 07:15 PM UTC

Table 1. Main features of the 12 global prediction systems in the S2S database.

S2S model	Time range (days)	Grid resolution	Hindcast frequency	Hindcast period	Ensemble size	Model version year
BoM	62	144 × 72	6 per month	1981–2013	33	2014
CMA	60	240 × 121	2 per week	2005–19	4	2020
CNR-ISAC	31	240 × 121	Every 5 days	1981–2010	5	2017
CNRM	47	240 × 121	Weekly	1993–2017	10	2019
ECCC	32	240 × 121	Weekly	1998–2017	4	2020
ECMWF	45	240 × 121	2 per week	1999–2018	11	2019
HMCR	61	240 × 121	Weekly	1985–2010	10	2020
JMA	33	240 × 121	2 per month	1981–2020	13	2021
KMA	60	240 × 121	4 per month	1991–2016	3	2021
NCEP	44	240 × 121	Daily	1999–2010	4	2011
UKMO	60	240 × 121	4 per month	1993–2016	7	2019
IAP-CAS	65	240 × 121	Daily	1999–2018	4	2019

b. ISV of EASM precipitation. The intraseasonal EASM precipitation mainly falls in the 12–40 day range (F. Liu et al. 2020, 2022). We identify the leading ISV mode by extracting the first empirical orthogonal function (EOF) mode of summer (May–September) 12–40-day bandpass-filtered precipitation over the EASM (20°–45°N, 100°–145°E) land regions. The Lanczos filter with 121 weights was used to perform the bandpass filtering (Duchon 1979).

c. ISV events. An ISV event was defined when the maxima or minima of 12–40-day bandpass-filtered EASM precipitation index (which will be defined later) anomaly were >0.5 standard deviation units for wet events or <−0.5 standard deviation units for dry events. The central day of an event, referred to as day 0, was determined as the day when the filtered precipitation index anomaly reached its peak or lowest point. Events primarily caused by exceptionally strong synoptic disturbances were excluded. This was done by excluding cases with the raw weekly precipitation index around day 0 below the climatology for wet events or above the climatology for dry events.

d. Compositing and significance. The correlation coefficient between predicted and observed weekly EASM precipitation index anomalies for any given day leading prediction was calculated using 840 ECMWF hindcasts for the summer season spanning from 1999 to 2018. The anomalies in observations and hindcasts were calculated relative to their respective daily climatology. The twice-per-week hindcast from the ECMWF is only available for Monday or Thursday, and thus the nearest hindcast to the target initial day was selected for each prediction. This selection process ensured a minimal bias of 1 day or no bias. Any prediction of ISV event that required a hindcast from Saturday was excluded from the analysis due to the hindcast's 2-day difference from the target initial day (Fig. 1 in the online supplemental material).

To represent the preceding signals of ISV events, time-lagged compositing was performed with respect to day 0 of each event. For subseasonal prediction evaluation, a correlation coefficient of 0.5 was used as the threshold to determine whether a prediction was skillful or not. For composites, a two-tailed Student's *t* test was used to test statistical significance. The Monte Carlo method with 10 000 iterations was used for testing the improvement of the prediction skill. For the filtered signal, the effective degree of freedom was considered to test the

Unauthenticated | Downloaded 11/22/24 07:15 PM UTC

significance (Zwiers and von Storch 1995), which is defined as $N_e = N(1-r1)/(1+r1)$, where N is the sample size of total days and $r1$ is the lag-one autocorrelation. The significance of multimodel mean prediction skill was tested using the smallest effective degree of freedom among the 12 models.

3. Results

a. Limited skill of S2S models in predicting subseasonal EASM precipitation. To evaluate the subseasonal prediction skill of weekly precipitation which is primarily dominated by predicting the ISV, we focused on the leading ISV mode of EASM precipitation. This mode exhibits a uniform spatial structure over southern EASM regions, encompassing areas south of the Yangtze River and western Japan (Fig. 1a). We used this EOF1 pattern in the observation to define the monsoon domain considered in this study. In both observations and predictions, the raw daily precipitation averaged over the southern EASM regions, i.e., the wet regions in Fig. 1a with precipitation anomalies >0.5 mm day^{-1}, was used to define the EASM precipitation index.

The multimodel mean of all 12 models displayed a skillful prediction of the weekly EASM precipitation index (Fig. 1b), measured by a correlation coefficient >0.5, only for 5 days in advance for all hindcasts. Notably, among all models, the ECMWF model exhibited the highest skill. However, even with its superior performance, the ECMWF model's skillful prediction extended only for up to 7 days, being consistent with previous findings of the limited

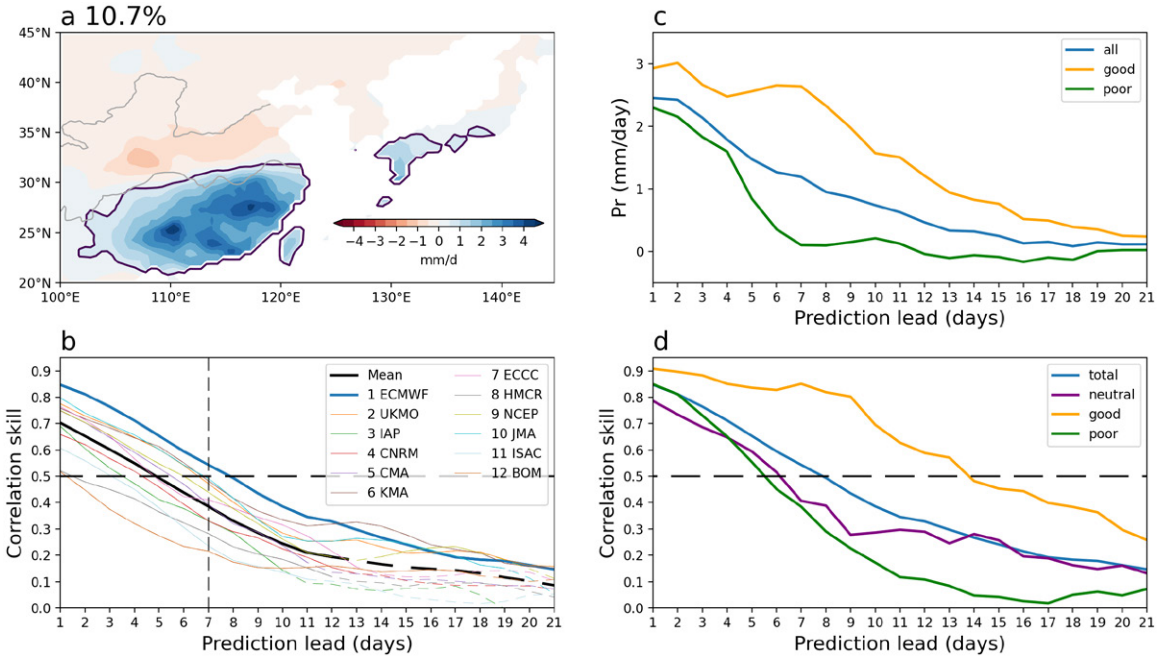

Fig. 1. EASM ISV and its prediction skill. (a) Leading mode of EASM ISV represented by the first EOF pattern of 12–40-day bandpass-filtered EASM (20°–45°N, 100°–145°E) land precipitation anomalies in CPC observation from 1979 to 2021. The upper and lower gray lines denote the Yellow and Yangtze rivers, respectively. The purple contour delineates the wet EASM regions with precipitation anomalies >0.5 mm day^{-1}. The percentage variance explained by this leading mode is marked on the panel. (b) Prediction skill of the weekly EASM precipitation index for 12 S2S models (colored lines) as a function of prediction lead days for their respective validation periods (Table 1). Black line denotes the multimodel mean. Solid lines denote significant (p < 0.01) skills. (c) ECMWF predicted event amplitude (mm day^{-1}) of EASM ISV averaged for all ISV events (blue line), well-predicted events (orange line), and poorly predicted events (green line). (d) ECMWF prediction skill of the weekly EASM precipitation index for all weeks [blue line, same as in (b)], weeks controlled by well-predicted (orange line) or poorly predicted (green line) ISV events, and weeks without any effect from ISV events (purple line).

Unauthenticated | Downloaded 11/22/24 07:15 PM UTC

subseasonal prediction skill for global land precipitation (Li and Robertson 2015; de Andrade et al. 2019; Liu et al. 2022; Singh et al. 2024). Here, a 7-day leading prediction of weekly precipitation refers to the prediction of the average precipitation for the seventh to thirteenth day from the initial time.

The subseasonal prediction skill of S2S models is expected to largely depend on their ability to capture the strong EASM ISV events. According to the definition presented in the method section, the EASM precipitation index was used to define the ISV events (Fig. 2a). There were 440 EASM ISV events during the period 1979–2021 (Fig. 2b). Supplemental Table 1 presented the top 30 wet and 30 dry events based on their rankings. During the period when ECMWF hindcasts were available (1999–2018), a total of 228 strong EASM ISV events, including both wet and dry events, were observed.

The amplitude of an ISV event was defined as the weekly EASM precipitation index anomaly relative to climatology spanning day 0, with the sign reversed for dry events that had negative precipitation anomalies. The 228 events from 1999 to 2018 displayed an average amplitude of 3.2 mm day^{-1} in observations, approximately half of the seasonal mean precipitation which stands at 6.0 mm day^{-1}. The wet events were stronger than the dry events, with average amplitudes of 3.6 and 2.7 mm day^{-1}, respectively. Overall, the ECMWF model initially captures the average ISV event amplitude for the first 2 days, but the predicted ISV amplitude quickly declined as forecast lead time increased, resulting in an average predicted

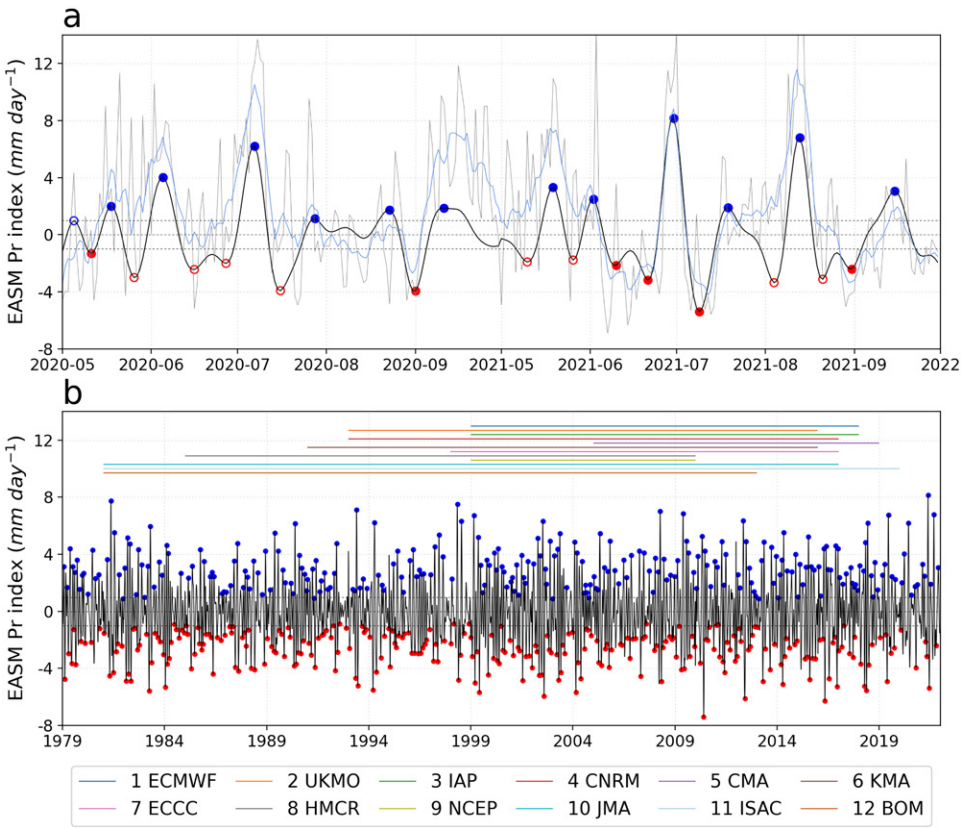

Fig. 2. Selection of ISV events from observations. Time series of EASM precipitation index anomaly (gray line), its 12–40-day component (black line), and 7-day running mean (blue line) for (a) 2020–21 summers and (b) 1979–2021 summers in the observation of CPC. Blue and red dots denote centers (day 0) of wet and dry ISV events, respectively. An ISV event is defined when the extrema of the 12–40-day-filtered EASM precipitation index anomaly are >0.5 standard deviation units for a wet event or <–0.5 standard deviation units for a dry event; events (circles) having a raw weekly precipitation index centered at day 0 below the climatology for wet events, and above the climatology for dry events, are removed (see methods). The hindcast periods of the 12 S2S models are also listed, represented by colored horizontal lines in (b).

Unauthenticated | Downloaded 11/22/24 07:15 PM UTC

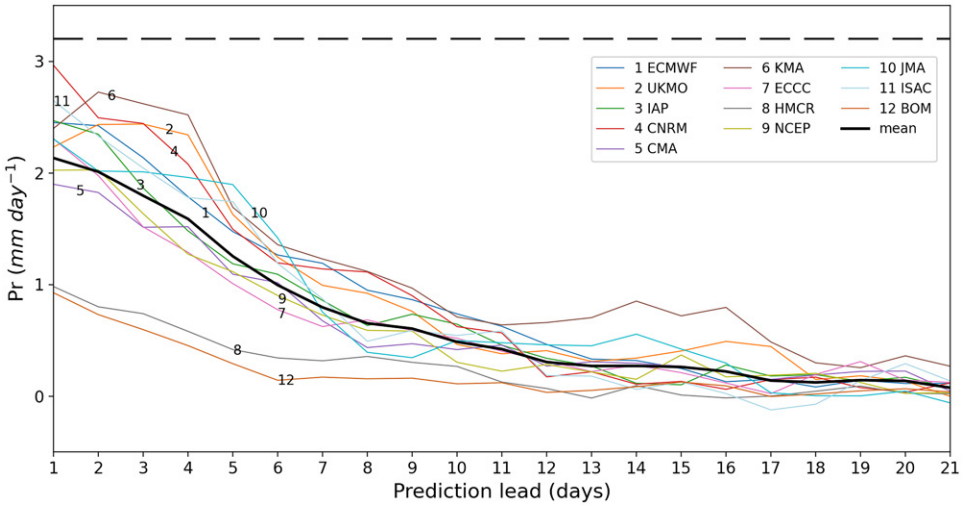

Fig. 3. Predicted EASM ISV event amplitude in S2S models. Prediction of EASM ISV event amplitude (mm day^{-1}) averaged for all EASM ISV events in each of the 12 S2S models (colored lines) for their own validation periods (Table 1), as well as their multimodel mean (black line). The dashed horizontal line denotes the average amplitude (3.2 mm day^{-1}) for all observed ISV events from 1999 to 2018. For each event, the amplitude is defined as the weekly EASM precipitation index anomaly with respect to climatology, with the sign reversed for dry events.

ISV amplitude of 1.2 mm day^{-1} for a 7-day forecast (Fig. 1c). Similarly, other 11 models also exhibited lower predicted ISV amplitude compared to the observations (Fig. 3).

b. Well-predicted and poorly predicted ISV events. To unravel the causes of the underestimation of ISV amplitude in model prediction, we defined a "prediction score" that represents the ratio of predicted to observed ISV amplitude for each event at a given forecast lead time. A higher score indicates better prediction for an event, while a negative score signifies model's incorrect prediction of the ISV phase. A well-predicted event required a prediction score >0.5; otherwise, it was defined as a poorly predicted event. Different threshold selections of prediction score did not qualitatively change our results. Among the 228 strong ISV events observed during the period 1999–2018, we identified 98 (43%) well-predicted events and 130 (57%) poorly predicted events based on the 7-day leading prediction score of the ECMWF model. As depicted in Fig. 1c, the ECMWF model predicted apparently higher ISV amplitude for well-predicted events compared to poorly predicted events.

To explore the subseasonal prediction skill of weekly EASM precipitation index anomalies associated with different strong ISV events, we categorized the targeted weeks in all hindcasts into three groups: those dominated by 1) well-predicted ISV events, 2) poorly predicted ISV events, and 3) weeks without any strong ISV events. A targeted week was defined as a strong ISV-dominated week if it encompassed day 0, i.e., the central day, of an ISV event.

For the weeks without any observed ISV events, which accounted for approximately 49% of the study period and are less likely to cause flood and heat wave disasters, the ECMWF model's forecast skill for precipitation was limited to six days. However, for ISV-dominated weeks, the ECMWF model demonstrated a much better precipitation forecast skill for well-predicted events compared to poorly predicted events (Fig. 1d). The skillful prediction, indicated by a correlation coefficient >0.5, was extended from 5 days for poorly predicted events to 13 days for well-predicted events. For 1-week leading prediction, the average prediction skill of the ECMWF model for well-predicted events (with a correlation coefficient of 0.85) is more than double that for poorly predicted events (0.38).

Unauthenticated | Downloaded 11/22/24 07:15 PM UTC

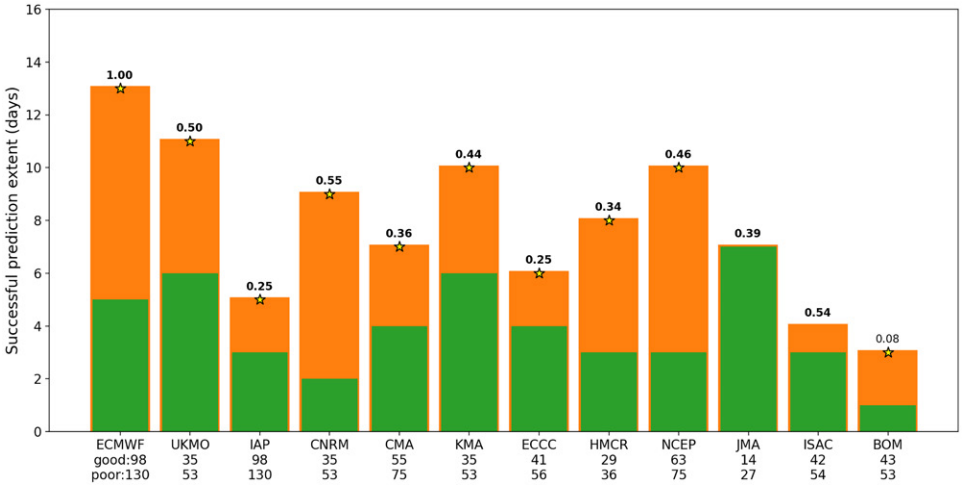

Fig. 4. ISV event–dependent subseasonal prediction skill. Longer prediction extent for skillful prediction of the weekly EASM precipitation index from control by well-predicted (orange bars) than by poorly predicted (green bars) events in all 12 S2S models. These well- and poorly predicted ISV events are defined based on ECMWF prediction, and only the periods that overlap with ECMWF prediction are analyzed in the other models. Stars indicate significant improvement ($p < 0.05$) based on the Monte Carlo method with 10 000 iterations. The prediction extent is defined by the last day on which the correlation coefficient is >0.5. Correlation (number over the bar) of 7-day leading prediction scores for all overlapped ISV events between ECMWF and each of the other models is also listed, with significant ($p < 0.05$) correlations highlighted in bold type. The numbers of overlapped well- and poorly predicted ISV events are listed below the name of each model.

In most of the other 11 S2S models, the prediction skills for weekly EASM precipitation, particularly for events classified as well predicted compared to those classified as poorly predicted based on the ECMWF prediction, were markedly higher (Fig. 4). Furthermore, for the ISV events predicted by both ECMWF and other models, a significant correlation was also observed between ECMWF and most of the other models for 7-day leading prediction scores. These results suggest that when one ISV event is accurately predicted by the ECMWF model, it also exhibits better prediction performance in other S2S models. In other words, the subseasonal prediction skill of EASM precipitation, regardless of S2S prediction models, depends on the characteristics of the ISV event itself.

c. Preceding signals of the well-predicted and poorly predicted events. It is hypothesized that these well-predicted and poorly predicted ISV events have different preceding signals, which could be used to identify the OBs for predicting each event. The observed preceding signals in OLR and 200-hPa winds were used to, respectively, detect the tropical and extratropical origins for EASM ISV. On day 0, which corresponds to the central day of each event and the peak phase of EASM ISV, the OLR composite centers over the southern EASM regions, aligning with the precipitation anomalies of the selected ISV events (Fig. 5).

In the case of well-predicted events, there was a notable emergence of enhanced convection, characterized by a southwest–northeast-tilted rainband anomaly (Fig. 5a). On day –12, this enhanced convection originated from the western North Pacific, covering the South China Sea and Philippine Sea. The enhanced convection system, coupled with low-level cyclonic wind anomalies (supplemental Fig. 2), propagated northwestward and was followed by suppressed convection to its southeast, forming a northwestward-propagating wave train. By approximately day –4, the enhanced convection started approaching East Asia and reached its peak over southern EASM regions on day 0. This northwestward-propagating tropical mode, often termed as the tropical quasi-biweekly oscillation (Lau and Lau 1990), is a convectively coupled Rossby wave (Wang and Xie 1997; Kikuchi and Wang 2009; Kiladis et al. 2009).

Unauthenticated | Downloaded 11/22/24 07:15 PM UTC

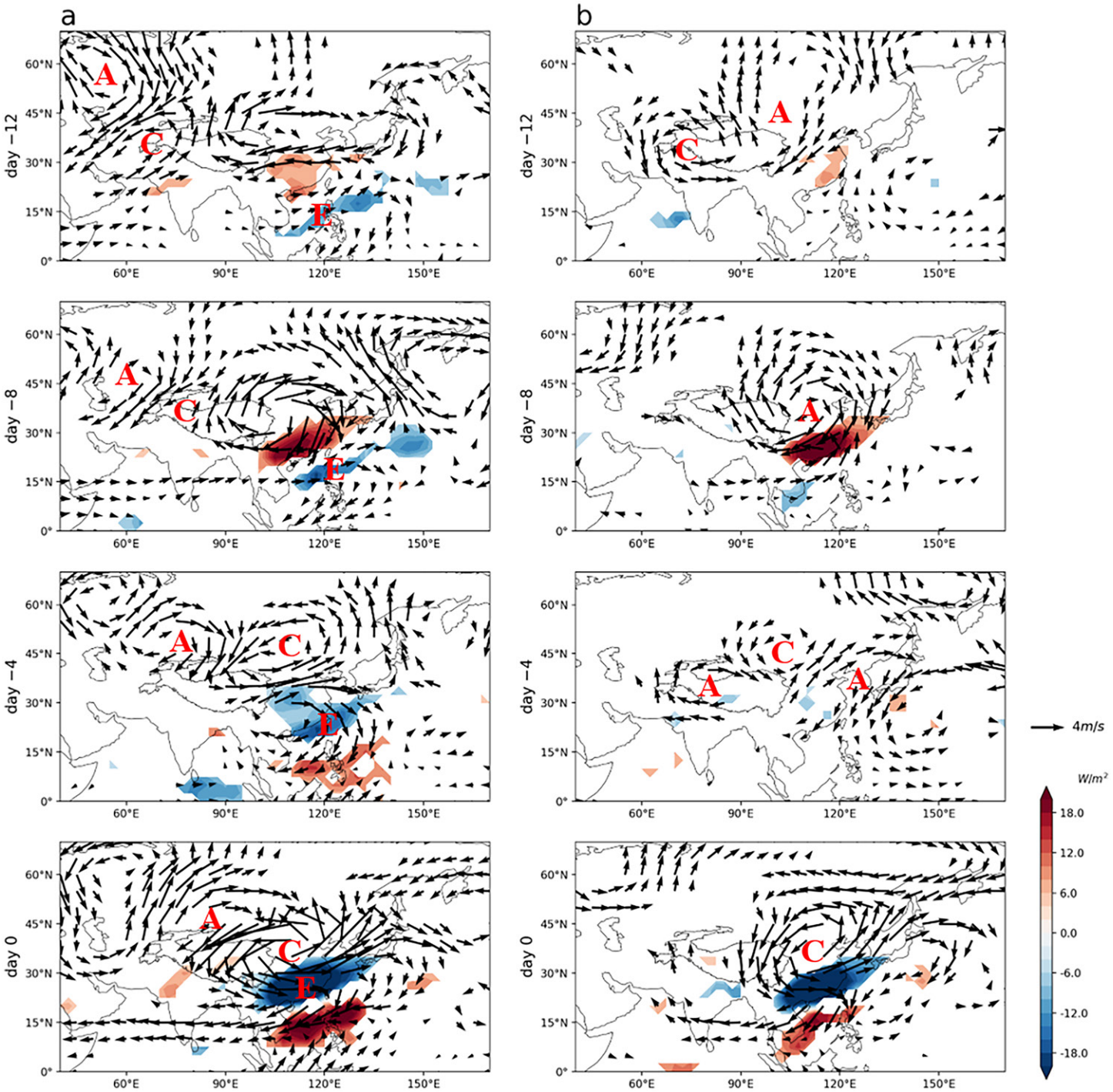

Fig. 5. Spatiotemporal structure of well- and poorly predicted events of EASM ISV. Time lagged-composite maps, from day −12 to day 0 using 4-day time increments, of 12–40-day filtered OLR anomalies (shading) and 200-hPa wind anomalies (vector) with respect to (a) 98 well-predicted and (b) 130 poorly predicted ISV events based on ECMWF prediction for boreal summers of 1999–2018. Day 0 denotes the peak of each event, and the signs of dry events are reversed for composite. Only significant ($p < 0.05$) OLR and wind anomalies based on the Student's *t* test are shown. Letters A and C track the centers of the anomalous extratropical anticyclone and cyclone, respectively, whereas E tracks the center of enhanced tropical convection, as indicated by the negative OLR anomaly.

A significant preceding signal was also observed in the extratropical region. On day −12, an upper-level anticyclonic–cyclonic wave train was observed between the East European Plain and Iranian Plateau, which then propagated eastward to the north of the Tibetan Plateau, mimicking the well-known Eurasian wave train (Wallace and Gutzler 1981; Barnston and Livezey 1987) on the subseasonal time scale (Zhu et al. 2023). By day −4, this upper-level cyclonic anomaly reached the Mongolian Plateau, before proceeding southeastward and intensifying

Unauthenticated | Downloaded 11/22/24 07:15 PM UTC

over northern China by day 0. The presence of the cyclonic anomaly over northern China could cause upward motion over southern EASM regions due to upper-level divergence induced by vorticity advection (Watanabe and Yamazaki 2012; Li and Mao 2019), which consequently contributed to increased EASM precipitation in these areas.

For the poorly predicted events, no significant tropical precursor was identified (Fig. 5b). Suppressed convection only appeared over the South China Sea on day 0, and it is likely a consequence rather than a precursor of the enhanced EASM precipitation. However, a notable preceding signal was observed in the extratropical region. On day −12, an upper-tropospheric cyclonic–anticyclonic wave train appeared between the western Tibetan Plateau and Mongolian Plateau. The anticyclonic anomaly then propagated southeastwards and centered over northern China on day −8, resulting in a decrease in EASM precipitation. Another reversed wave train (anticyclonic–cyclonic) was observed over the western Tibetan Plateau–Mongolian Plateau on day −4. This wave train led to the same southeastward propagation of the upper-level cyclonic anomaly and a subsequent increase in EASM precipitation by day 0.

A day-by-day composite of the upper-level signals preceding these poorly predicted ISV events reveals a westward-propagating anomalous anticyclonic high observed in the southern part of northern China from day −8 (supplemental Fig. 3). Subsequently, starting on day −5, an anticyclonic anomaly developed over the western Tibetan Plateau, accompanied by the development of a cyclonic anomaly over the Mongolian Plateau. This westward propagation of high pressure-controlled Rossby wave occurred at latitudes of approximately 30°–40°N, south of the climatic westerly jet. Such westward propagation of Rossby waves is due to the absence of the Doppler shift effect of the climatic westerly jet. The impact of EASM on the western Tibetan Plateau through the westward-propagating Rossby waves was also documented in a simulation study (Zhang et al. 2016), although it was on the interannual time scale.

Figure 6a summarizes the origins and pathways of the preceding signals of well- and poorly predicted ISV events of EASM precipitation. The pathways of well-predicted events were connected by upper-tropospheric anomaly centers from the East European Plain through the Mongolian Plateau to northern China. Additionally, tropical convection centers from the western North Pacific to East Asia also play a significant role in the development of these events. The poorly predicted events, however, originate from the upper-level cyclonic anomaly that extends from the western Tibetan Plateau through the Mongolian Plateau to northern China, exacerbated by feedback from the westward propagation of the northern China anticyclonic anomaly.

d. OBs for skillful subseasonal prediction of EASM precipitation. As mentioned above, the subseasonal prediction skill of EASM precipitation is ISV event dependent. Thus, the notable differences of observed preceding signals between the well- and poorly predicted ISV events provide us an opportunity to assess the predictability of forthcoming events in advance. We hypothesized that the prediction skill of EASM precipitation is determined by the propagation stability of the ISV origins, namely, the stability of the preceding wave trains during their propagation. To quantify this, we introduced a wave train index, which was defined as the strength of the wave center along its propagation path for a given specific day, and the propagation stability could be estimated by the correlation between the preceding wave train index for a specific leading day and day 0. A higher propagation stability implied that the preceding wave train propagates steadily and is, therefore, more predictable.

The preceding wave train indices for both observed and simulated ISV events were defined based on the observed composite map (Fig. 5). On day −4, the Eurasian wave train was comprised of an upper-level Novosibirsk Plain anticyclone and Mongolian Plateau cyclone; thus, the Eurasian wave train index (I_{-4}) was defined as the difference between the 200-hPa averaged geopotential height anomalies in the anticyclonic "A" region ($H_{A\text{-}4}$) and those in

Unauthenticated | Downloaded 11/22/24 07:15 PM UTC

the cyclonic "C" region ($H_{C\text{-}4}$) for well-predicted ISV events, i.e., $I_{-4} = H_{A\text{-}4} - H_{C\text{-}4}$. The western Tibetan Plateau wave train index was defined in the same way, but it was based on the composite map for poorly predicted ISV events.

On day 0, we only considered the cyclonic anomaly over northern China ($I_0 = -H_{C0}$) for both the Eurasian and western Tibetan Plateau wave trains, since the anticyclonic anomaly was so weak for the western Tibetan Plateau wave train. The tropical wave train index was defined as the difference between the averaged OLR anomalies in the enhanced convection "E" region and those in the suppressed convection region to its southeast side for well-predicted events. A threshold of 0.6 times the maximum anomalies was used to select these regions in Fig. 5, and different choices of the threshold did not qualitatively change our results.

The propagation stability was defined by the correlation coefficient between the wave train index for any k-leading day (I_{-k}) and the reference day 0 (I_0) during boreal summer in observation from 1979 to 2021 and in models for their hindcast periods. The calculation procedure of this propagation stability is shown in supplemental Fig. 5.

Here, we took the propagation stability from day −4 to day 0 as an example. There was a strong correlation between the 7-day leading prediction skill of EASM weekly precipitation and the propagation stability among these 12 S2S models, with a correlation coefficient of 0.73 ($p < 0.01$) for the combined stability (through a multiple linear regression) of Eurasian and tropical wave trains (Fig. 6b) and 0.71 ($p < 0.01$) for the western Tibetan Plateau wave train (Fig. 6c). This result indicates that a higher stability of the ISV origin leads to a better prediction of EASM precipitation in S2S models.

The observed propagation stability of the western Tibetan Plateau wave train, from day −4 to day 0, was 0.41 ($p < 0.01$), which was weaker than the combined stability of Eurasian and tropical wave trains (0.47; $p < 0.01$) and much weaker compared to that of the Eurasian wave train alone (0.56; $p < 0.01$). Moreover, for a longer leading period of day −12, the propagation

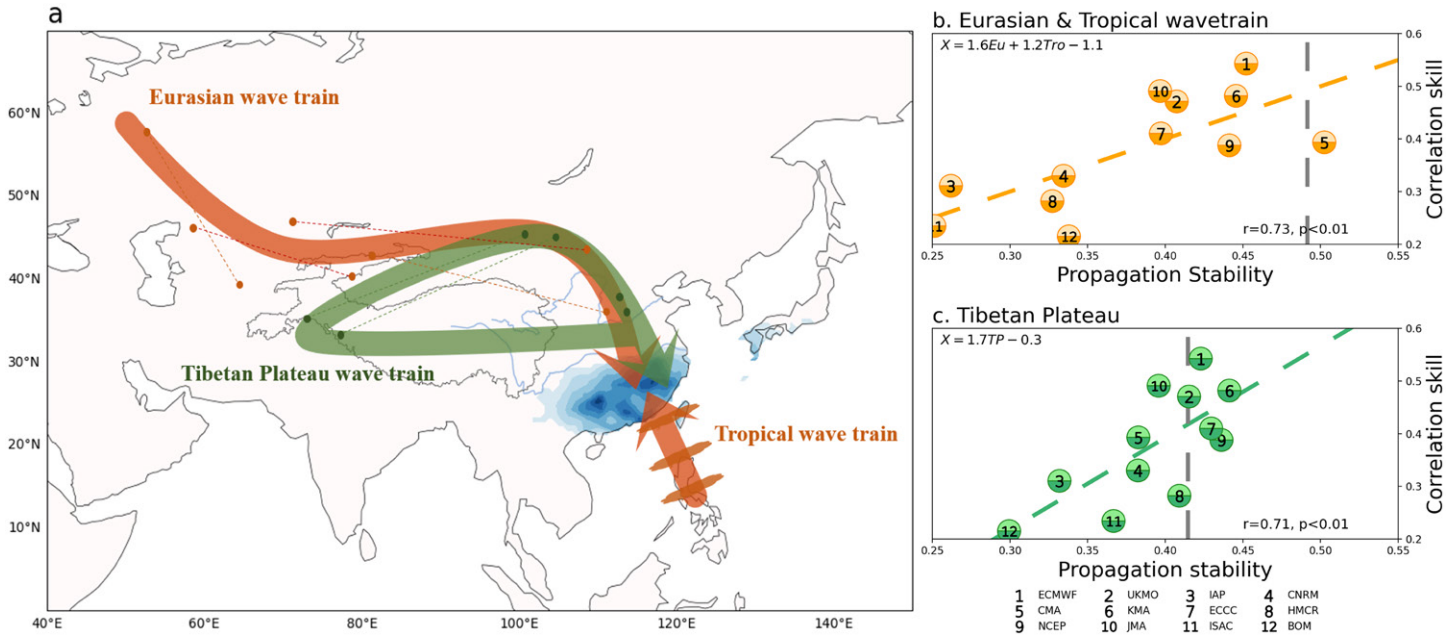

Fig. 6. Propagation stability of EASM ISV origins. (a) Schematic diagram of EASM ISV origins (arrows) from Eurasian and tropical wave trains for well-predicted (orange) ISV events and from a western Tibetan Plateau wave train for poorly predicted (green) events. The preceding upper-tropospheric cyclonic–anticyclonic centers (connected by dashed lines) and convection centers from day −12 to day 0 on Fig. 5 are indicated by dots and clouds, respectively. (b) Relationship between the 7-day leading prediction skill of the weekly EASM precipitation index and propagation stability of the combination (through a multiple linear regression) of Eurasian and tropical wave trains in all 12 S2S models. Orange dashed line shows the linear regression with a significant correlation coefficient *r* and *p* value. Observed propagation stability from 1979 to 2021 is also marked by a gray dashed line for reference. (c) As in (b), but for the western Tibetan Plateau wave train.

Unauthenticated | Downloaded 11/22/24 07:15 PM UTC

stability of the western Tibetan Plateau wave train sharply dropped to 0.24, which was notably weaker than those of the Eurasian (0.45; $p < 0.01$) and tropical (0.41; $p < 0.01$) wave trains.

The low propagation stability of the western Tibetan Plateau wave train acted as a barrier for skillful EASM subseasonal prediction, confining the prediction skill to only 1 week. However, the more stable Eurasian and tropical wave trains provided opportunities for achieving long-term skillful subseasonal prediction extending up to 13 days. Since the tropical and Eurasian wave trains only accounted for about half of the intraseasonal variance of EASM precipitation (Ren et al. 2022), only 43% of the ISV events could be well predicted by the ECMWF model.

The propagation stability of these tropical and extratropical origins in the 12 S2S models was generally found to be weaker compared to observations (Figs. 6b,c), especially for the models with low prediction skill (Figs. 1b and 3). This indicates that even if the models are able to simulate the cloud microphysics processes and precipitation, there is still room for improvement in the simulation of these preceding signals to enhance the prediction skill of ISV events. Alternatively, the imperfect precipitation simulation also limits the prediction skill. A clear example is the China Meteorological Administration (CMA) model that demonstrated the highest propagation stability for the Eurasian and tropical wave trains but exhibited low prediction skill for precipitation (Fig. 6b). This implies that the CMA model could benefit from further improvements in terms of precipitation parameterizations or from postprocessing approach using predicted circulation.

In this work, we focused on the weekly precipitation prediction. Different selections of intraseasonal bands such as 12–80 or 8–40 days or different prediction targets such as pentad or biweekly precipitation anomalies did not qualitatively change our results, although there were slight changes in the OBs (supplemental Figs. 6–8).

4. Discussion and conclusions

This study introduces a method to increase our confidence in achieving more accurate subseasonal prediction by identifying two key components: the opportunities and barriers. The central idea is to identify the types of ISV events in which the model exhibits high prediction skills (opportunities) and those in which the model's skills are limited (barriers). Identifying these OBs will help us gain confidence in predicting such events and acknowledge the limitations of predictability.

We focus on the complex EASM, where the average skillful prediction of weekly precipitation remains limited to a lead time of 1 week despite employing state-of-the-art dynamical prediction models. Prediction skill of the model for weekly precipitation anomalies is limited to 6 days when the target week does not include any strong ISV events. This indicates that the predictability of the EASM mainly comes from strong ISV events and suggests that we should focus on predicting ISV events in subseasonal predictions.

Our results further reveal that the subseasonal prediction skill heavily relies on the origins of each ISV event. Specifically, models demonstrate good prediction skills for ISV events originating from the tropical and Eurasian wave trains, while they perform poorly in predicting events originating from the western Tibetan Plateau wave train. The opportunity for skillful subseasonal prediction arises from the steady propagation of tropical and extratropical Eurasian wave trains, which enables a skillful prediction up to 13 days ahead for 43% of all events. However, the weak propagation stability of the Tibetan Plateau wave train, acting as a "Tibetan Plateau barrier," restricts the skillful prediction to within 5 days, even in the best-performing model (ECMWF).

Our work only focuses on identifying precursor signals in the troposphere. Numerous studies have demonstrated the influence of precursors such as soil moisture, snow cover, stratospheric circulation, and sea surface temperature on the ISV (Koster et al. 2011; DeMott

Unauthenticated | Downloaded 11/22/24 07:15 PM UTC

et al. 2015; Li et al. 2018; Domeisen et al. 2020; Mariotti et al. 2020). Although current dynamic prediction models struggle to precisely simulate them as effective precursors (Richter et al. 2024), an empirical model using machine learning methods, process improvement in dynamic models, or a combining dynamical and data-driven forecast (Bach et al. 2024) should benefit the identification of OBs for accurate prediction.

The approach used in this study to identify OBs for skillful prediction should also be applicable to other weather and climate systems and regions beyond the EASM area, if we can find explicit physical processes for the identified OBs, contributing to the Earth-System Prediction Initiative (Shapiro et al. 2010). For example, it is interesting to investigate whether the wave activities over the Eurasian continent and Tibetan Plateau act as opportunities or barriers for the seasonal prediction of EASM, as they have been found to have a significant impact on EASM precipitation (Liu et al. 2007; Jiang et al. 2022; Liu et al. 2023). In practical prediction, by examining the signals preceding the initial time, we can assess the likelihood of the model yielding either favorable or unfavorable predictions based on their resemblance to the OBs. When the prediction system raises an alarm for an upcoming disaster event, we need to go back and check if there were any signals resemble the opportunities in observation prior to the prediction. If such resemblances are noticed, we should enhance our confidence in making more accurate predictions and raise alarms for potential disasters.

Acknowledgments. F. L. and W. D. are supported by the National Natural Science Foundation of China (U21A6001), Guangdong Major Project of Basic and Applied Basic Research (Grant 2020B0301030004), and the National Natural Science Foundation of China (42175061). B. W. acknowledges the support from NSF/Climate Dynamics Award 2025057. This paper is WEPRE publication 001.

Data availability statement. All data used in this study were obtained from publicly available sources. The S2S database can be accessed from https://apps.ecmwf.int/datasets/data/s2s. NCEP Reanalysis II dataset can be downloaded at https://psl.noaa.gov/data/gridded/data.ncep.reanalysis2.html. The NOAA OLR is available at https://psl.noaa.gov/data/gridded/data.olrcdr.interp.html. CPC Global Unified Gauge-Based Analysis of Daily Precipitation is available at https://www.psl.noaa.gov/data/gridded/data.cpc.globalprecip.html.

Unauthenticated | Downloaded 11/22/24 07:15 PM UTC

References

Bach, E., V. Krishnamurthy, S. Mote, J. Shukla, A. S. Sharma, E. Kalnay, and M. Ghil, 2024: Improved subseasonal prediction of South Asian monsoon rainfall using data-driven forecasts of oscillatory modes. *Proc. Natl. Acad. Sci. USA*, **121**, e2312573121, https://doi.org/10.1073/pnas.2312573121.

Barnston, A. G., and R. E. Livezey, 1987: Classification, seasonality and persistence of low-frequency atmospheric circulation patterns. *Mon. Wea. Rev.*, **115**, 1083–1126, https://doi.org/10.1175/1520-0493(1987)115<1083:CSAPOL>2.0.CO;2.

Chen, L., C. Zhu, W. Wang, and P. Zhang, 2001: Analysis of the characteristics of 30–60 day low-frequency oscillation over Asia during 1998 SCSMEX. *Adv. Atmos. Sci.*, **18**, 623–638, https://doi.org/10.1007/s00376-001-0050-0.

de Andrade, F. M., C. A. S. Coelho, and I. F. A. Cavalcanti, 2019: Global precipitation hindcast quality assessment of the Subseasonal to Seasonal (S2S) prediction project models. *Climate Dyn.*, **52**, 5451–5475, https://doi.org/10.1007/s00382-018-4457-z.

DeMott, C. A., N. P. Klingaman, and S. J. Woolnough, 2015: Atmosphere-ocean coupled processes in the Madden-Julian oscillation. *Rev. Geophys.*, **53**, 1099–1154, https://doi.org/10.1002/2014RG000478.

Ding, Y., Y. Liu, and Z.-Z. Hu, 2021: The record-breaking Mei-yu in 2020 and associated atmospheric circulation and tropical SST anomalies. *Adv. Atmos. Sci.*, **38**, 1980–1993, https://doi.org/10.1007/s00376-021-0361-2.

Domeisen, D. I. V., and Coauthors, 2020: The role of the stratosphere in subseasonal to seasonal prediction: 2. Predictability arising from stratosphere-troposphere coupling. *J. Geophys. Res. Atmos.*, **125**, e2019JD030923, https://doi.org/10.1029/2019JD030923.

Duchon, C. E., 1979: Lanczos filtering in one and two dimensions. *J. Appl. Meteor.*, **18**, 1016–1022, https://doi.org/10.1175/1520-0450(1979)018<1016:LFIOAT>2.0.CO;2.

Gao, M., J. Yang, B. Wang, S. Zhou, D. Gong, and S.-J. Kim, 2018: How are heat waves over Yangtze River valley associated with atmospheric quasi-biweekly oscillation? *Climate Dyn.*, **51**, 4421–4437, https://doi.org/10.1007/s00382-017-3526-z.

He, C., T. Zhou, L. Zhang, X. Chen, and W. Zhang, 2023: Extremely hot East Asia and flooding western South Asia in the summer of 2022 tied to reversed flow over Tibetan Plateau. *Climate Dyn.*, **61**, 2103–2119, https://doi.org/10.1007/s00382-023-06669-y.

Hirockawa, Y., T. Kato, K. Araki, and W. Mashiko, 2020: Characteristics of an extreme rainfall event in Kyushu district, southwestern Japan in early July 2020. *SOLA*, **16**, 265–270, https://doi.org/10.2151/sola.2020-044.

Hsu, P.-C., J.-Y. Lee, and K.-J. Ha, 2016: Influence of boreal summer intraseasonal oscillation on rainfall extremes in southern China. *Int. J. Climatol.*, **36**, 1403–1412, https://doi.org/10.1002/joc.4433.

Jiang, J., T. Su, Y. Liu, G. Wu, W. Yu, and J. Li, 2022: Southeast China extreme drought event in August 2019: Context of coupling of midlatitude and tropical systems. *J. Climate*, **35**, 7299–7313, https://doi.org/10.1175/JCLI-D-22-0138.1.

——, Y. Liu, J. Mao, and G. Wu, 2023: Extreme heatwave over eastern China in summer 2022: The role of three oceans and local soil moisture feedback. *Environ. Res. Lett.*, **18**, 044025, https://doi.org/10.1088/1748-9326/acc5fb.

Kanamitsu, M., W. Ebisuzaki, J. Woollen, S.-K. Yang, J. J. Hnilo, M. Fiorino, and G. L. Potter, 2002: NCEP–DOE AMIP-II Reanalysis (R-2). *Bull. Amer. Meteor. Soc.*, **83**, 1631–1644, https://doi.org/10.1175/BAMS-83-11-1631.

Kikuchi, K., and B. Wang, 2009: Global perspective of the quasi-biweekly oscillation. *J. Climate*, **22**, 1340–1359, https://doi.org/10.1175/2008JCLI2368.1.

Kiladis, G. N., M. C. Wheeler, P. T. Haertel, K. H. Straub, and P. E. Roundy, 2009: Convectively coupled equatorial waves. *Rev. Geophys.*, **47**, RG2003, https://doi.org/10.1029/2008RG000266.

KMA, 2021: Abnormal Climate Report 2020 (in Korean). KMA, 212 pp., https://www.climate.go.kr/home/bbs/view.php?code=93&bname=abnormal&vcode=6494.

Koster, R. D., and Coauthors, 2011: The second phase of the global land–atmosphere coupling experiment: Soil moisture contributions to subseasonal forecast skill. *J. Hydrometeor.*, **12**, 805–822, https://doi.org/10.1175/2011JHM1365.1.

Lau, K.-H., and N.-C. Lau, 1990: Observed structure and propagation characteristics of tropical summertime synoptic scale disturbances. *Mon. Wea. Rev.*, **118**, 1888–1913, https://doi.org/10.1175/1520-0493(1990)118<1888:OSAPCO>2.0.CO;2.

Li, J., and J. Mao, 2019: Coordinated influences of the tropical and extratropical intraseasonal oscillations on the 10–30-day variability of the summer rainfall over southeastern China. *Climate Dyn.*, **53**, 137–153, https://doi.org/10.1007/s00382-018-4574-8.

Li, S., and A. W. Robertson, 2015: Evaluation of submonthly precipitation forecast skill from global ensemble prediction systems. *Mon. Wea. Rev.*, **143**, 2871–2889, https://doi.org/10.1175/MWR-D-14-00277.1.

Li, W., W. Guo, B. Qiu, Y. Xue, P.-C. Hsu, and J. Wei, 2018: Influence of Tibetan Plateau snow cover on East Asian atmospheric circulation at medium-range time scales. *Nat. Commun.*, **9**, 4243, https://doi.org/10.1038/s41467-018-06762-5.

Liebmann, B., and C. A. Smith, 1996: Description of a complete (interpolated) outgoing longwave radiation dataset. *Bull. Amer. Meteor. Soc.*, **77**, 1275–1277.

Lim, E.-P., H. H. Hendon, G. Boschat, D. Hudson, D. W. J. Thompson, A. J. Dowdy, and J. M. Arblaster, 2019: Australian hot and dry extremes induced by weakenings of the stratospheric polar vortex. *Nat. Geosci.*, **12**, 896–901, https://doi.org/10.1038/s41561-019-0456-x.

Liu, F., Y. Ouyang, B. Wang, J. Yang, J. Ling, and P.-C. Hsu, 2020: Seasonal evolution of the intraseasonal variability of China summer precipitation. *Climate Dyn.*, **54**, 4641–4655, https://doi.org/10.1007/s00382-020-05251-0.

——, B. Wang, Y. Ouyang, H. Wang, S. Qiao, G. Chen, and W. Dong, 2022: Intraseasonal variability of global land monsoon precipitation and its recent trend. *npj Climate Atmos. Sci.*, **5**, 30, https://doi.org/10.1038/s41612-022-00253-7.

Liu, Y., B. Hoskins, and M. Blackburn, 2007: Impact of Tibetan orography and heating on the summer flow over Asia. *J. Meteor. Soc. Japan*, **85B**, 1–19, https://doi.org/10.2151/jmsj.85B.1.

——, M. Lu, H. Yang, A. Duan, B. He, S. Yang, and G. Wu, 2020: Land–atmosphere–ocean coupling associated with the Tibetan Plateau and its climate impacts. *Natl. Sci. Rev.*, **7**, 534–552, https://doi.org/10.1093/nsr/nwaa011.

——, L. Luan, G. Wu, and T. Ma, 2023: Impacts of the surface potential vorticity circulation over the Tibetan Plateau on the East Asian monsoon in July. *Atmosphere*, **14**, 1038, https://doi.org/10.3390/atmos14061038.

Mao, J., and J. C. L. Chan, 2005: Intraseasonal variability of the South China Sea summer monsoon. *J. Climate*, **18**, 2388–2402, https://doi.org/10.1175/JCLI3395.1.

Mariotti, A., and Coauthors, 2020: Windows of opportunity for skillful forecasts subseasonal to seasonal and beyond. *Bull. Amer. Meteor. Soc.*, **101**, E608–E625, https://doi.org/10.1175/BAMS-D-18-0326.1.

Meehl, G. A., and C. Tebaldi, 2004: More intense, more frequent, and longer lasting heat waves in the 21st century. *Science*, **305**, 994–997, https://doi.org/10.1126/science.1098704.

National Academies of Sciences, Engineering, and Medicine, 2016: *Next Generation Earth System Prediction: Strategies for Subseasonal to Seasonal Forecasts.* National Academies Press, 335 pp.

Park, C., and Coauthors, 2021: Record-breaking summer rainfall in South Korea in 2020: Synoptic characteristics and the role of large-scale circulations. *Mon. Wea. Rev.*, **149**, 3085–3100, https://doi.org/10.1175/MWR-D-21-0051.1.

Ren, Q., F. Liu, B. Wang, S. Yang, H. Wang, and W. Dong, 2022: Origins of the intraseasonal variability of East Asian summer precipitation. *Geophys. Res. Lett.*, **49**, e2021GL096574, https://doi.org/10.1029/2021GL096574.

Unauthenticated | Downloaded 11/22/24 07:15 PM UTC

Richter, J. H., and Coauthors, 2024: Quantifying sources of subseasonal prediction skill in CESM2. *npj Climate Atmos. Sci.*, **7**, 59, https://doi.org/10.1038/s41612-024-00595-4.

Shapiro, M., and Coauthors, 2010: An Earth-system prediction initiative for the twenty-first century. *Bull. Amer. Meteor. Soc.*, **91**, 1377–1388, https://doi.org/10.1175/2010BAMS2944.1.

Sheng, B., H. Wang, H. Li, K. Wu, and Q. Li, 2023: Thermodynamic and dynamic effects of anomalous dragon boat water over South China in 2022. *Wea. Climate Extremes*, **40**, 100560, https://doi.org/10.1016/j.wace.2023.100560.

Sigmond, M., J. F. Scinocca, V. V. Kharin, and T. G. Shepherd, 2013: Enhanced seasonal forecast skill following stratospheric sudden warmings. *Nat. Geosci.*, **6**, 98–102, https://doi.org/10.1038/ngeo1698.

Singh, B., M. A. Ehsan, and A. W. Robertson, 2024: Calibrated probabilistic subseasonal forecasting for Pakistan's monsoon rainfall in 2022. *Climate Dyn.*, **62**, 3375–3393, https://doi.org/10.1007/s00382-023-07071-4.

Stan, C., D. M. Straus, J. S. Frederiksen, H. Lin, E. D. Maloney, and C. Schumacher, 2017: Review of tropical-extratropical teleconnections on intraseasonal time scales. *Rev. Geophys.*, **55**, 902–937, https://doi.org/10.1002/2016RG000538.

Takaya, Y., I. Ishikawa, C. Kobayashi, H. Endo, and T. Ose, 2020: Enhanced Meiyu-Baiu rainfall in early summer 2020: Aftermath of the 2019 super IOD event. *Geophys. Res. Lett.*, **47**, e2020GL090671, https://doi.org/10.1029/2020GL090671.

Vitart, F., and Coauthors, 2017: The Subseasonal to Seasonal (S2S) prediction project database. *Bull. Amer. Meteor. Soc.*, **98**, 163–173, https://doi.org/10.1175/BAMS-D-16-0017.1.

Wallace, J. M., and D. S. Gutzler, 1981: Teleconnections in the geopotential height field during the Northern Hemisphere winter. *Mon. Wea. Rev.*, **109**, 784–812, https://doi.org/10.1175/1520-0493(1981)109<0784:TITGHF>2.0.CO;2.

Wang, B., and X. Xie, 1997: A model for the boreal summer intraseasonal oscillation. *J. Atmos. Sci.*, **54**, 72–86, https://doi.org/10.1175/1520-0469(1997)054<0072:AMFTBS>2.0.CO;2.

Watanabe, T., and K. Yamazaki, 2012: Influence of the anticyclonic anomaly in the subtropical jet over the western Tibetan Plateau on the intraseasonal variability of the summer Asian monsoon in early summer. *J. Climate*, **25**, 1291–1303, https://doi.org/10.1175/JCLI-D-11-00036.1.

Webster, P. J., and C. Hoyos, 2004: Prediction of monsoon rainfall and river discharge on 15–30-day time scales. *Bull. Amer. Meteor. Soc.*, **85**, 1745–1766, https://doi.org/10.1175/BAMS-85-11-1745.

Wei, K., C. Ouyang, H. Duan, Y. Li, M. Chen, J. Ma, H. An, and S. Zhou, 2020: Reflections on the catastrophic 2020 Yangtze River basin flooding in southern China. *Innovation*, **1**, 100038, https://doi.org/10.1016/j.xinn.2020.100038.

Xie, P., M. Chen, S. Yang, A. Yatagai, T. Hayasaka, Y. Fukushima, and C. Liu, 2007: A gauge-based analysis of daily precipitation over East Asia. *J. Hydrometeor.*, **8**, 607–626, https://doi.org/10.1175/JHM583.1.

Yang, J., B. Wang, B. Wang, and Q. Bao, 2010: Biweekly and 21–30-day variations of the subtropical summer monsoon rainfall over the lower reach of the Yangtze River basin. *J. Climate*, **23**, 1146–1159, https://doi.org/10.1175/2009JCLI3005.1.

——, Q. Bao, B. Wang, H. He, M. Gao, and D. Gong, 2017: Characterizing two types of transient intraseasonal oscillations in the eastern Tibetan Plateau summer rainfall. *Climate Dyn.*, **48**, 1749–1768, https://doi.org/10.1007/s00382-016-3170-z.

Zhang, C., 2013: Madden–Julian oscillation: Bridging weather and climate. *Bull. Amer. Meteor. Soc.*, **94**, 1849–1870, https://doi.org/10.1175/BAMS-D-12-00026.1.

Zhang, P., Y. Liu, and B. He, 2016: Impact of East Asian summer monsoon heating on the interannual variation of the South Asian high. *J. Climate*, **29**, 159–173, https://doi.org/10.1175/JCLI-D-15-0118.1.

Zhu, T., J. Yang, B. Wang, and Q. Bao, 2023: Boreal summer extratropical intraseasonal waves over the Eurasian continent and real-time monitoring metrics. *J. Climate*, **36**, 3971–3991, https://doi.org/10.1175/JCLI-D-22-0788.1.

Zwiers, F. W., and H. von Storch, 1995: Taking serial correlation into account in tests of the mean. *J. Climate*, **8**, 336–351, https://doi.org/10.1175/1520-0442(1995)008<0336:TSCIAI>2.0.CO;2.

Unauthenticated | Downloaded 11/22/24 07:15 PM UTC